Nano Research 2017, 10(3): 802–813
DOI 10.1007/s12274-016-1333-1
Research Article
ISSN 1998-0124
CN 11-5974/O4

Hierarchical graphene foam-based phase change materials with enhanced thermal conductivity and shape stability for efficient solar-to-thermal energy conversion and storage

Guoqiang Qi[1,2], Jie Yang[2], Ruiying Bao[2], Dongyun Xia[1], Min Cao[1], Wei Yang[2] (✉), Mingbo Yang[2], and Dacheng Wei[1] (✉)

[1] *State Key Laboratory of Molecular Engineering of Polymers, Department of Macromolecular Science, Fudan University, Shanghai 200433, China*
[2] *College of Polymer Science and Engineering, State Key Laboratory of Polymer Materials Engineering, Sichuan University, Chengdu 610065, China*

Received: 14 September 2016
Revised: 10 October 2016
Accepted: 12 October 2016

KEYWORDS
phase-change materials,
hierarchical graphene foam,
light-to-thermal energy conversion,
thermal conductivity,
solar energy

ABSTRACT

Recently, graphene foam (GF) with a three-dimensional (3D) interconnected network produced by template-directed chemical vapor deposition (CVD) has been used to prepare composite phase-change materials (PCMs) with enhanced thermal conductivity. However, the pore size of GF is as large as hundreds of micrometers, resulting in a remarkable thermal resistance for heat transfer from the PCM inside the large pores to the GF strut walls. In this study, a novel 3D hierarchical GF (HGF) is obtained by filling the pores of GF with hollow graphene networks. The HGF is then used to prepare a paraffin wax (PW)-based composite PCM. The thermal conductivity of the PW/HGF composite PCM is 87% and 744% higher than that of the PW/GF composite PCM and pure PW, respectively. The PW/HGF composite PCM also exhibits better shape stability than the PW/GF composite PCM, negligible change in the phase-change temperature, a high thermal energy storage density that is 95% of pure PW, good thermal reliability, and chemical stability with cycling for 100 times. More importantly, PW/HGF composite PCM allows light-driven thermal energy storage with a high light-to-thermal energy conversion and storage efficiency, indicating its great potential for applications in solar-energy utilization and storage.

1 Introduction

Phase change materials (PCMs) are among the most significant advanced energy-saving materials. They are capable of storing and releasing a large amount of thermal energy in the form of latent heat during

Address correspondence to Dacheng Wei, weidc@fudan.edu.cn; Wei Yang, weiyang@scu.edu.cn

solid–liquid and liquid–solid phase changes, and they have found widespread applications in the thermal management and storage fields [1–8]. However, most PCMs exhibit an inherent low thermal conductivity, which decreases the efficiency of the thermal storage device. Various carbonaceous materials have been employed to improve the heat transfer of PCMs because of their intrinsically high thermal conductivities [9–14]. Nevertheless, only a modest increase in thermal conductivity can be achieved in composite PCMs employing these dispersed fillers, even at a high loading, which significantly reduces the thermal energy storage density because the portion of the working substance is replaced by the incorporated fillers. In these composite PCMs, the thermal conductivity is limited by the random contact geometry and weak physical interactions of the fillers, resulting in a large contact thermal resistance at junctions between the fillers.

Recently, three-dimensional (3D) graphene foam (GF) has been synthesized by Ni foam template-directed chemical vapor deposition (CVD) [15]. In contrast to graphene aerogels obtained by self-assembling small pieces of chemically derived graphene sheets via weak physical interactions, such as the van der Waals force, hydrogen bonding, and π–π stacking [16, 17], which still lead to a pronounced interfacial thermal resistance bottleneck, GF fabricated by CVD is a monolith of a graphene 3D network that provides continuous pathways for phonon transport with a small resistance through the high-quality and continuous CVD-grown graphene building blocks [18]. Such a continuous GF monolith with a high basal-plane solid thermal conductivity of graphene has been embedded in a PCM to act as a thermal conductive filler for phonon transport [5]. The thermal conductivity of the resulting composite PCM increased significantly with negligible change in other performance criteria. However, the pore size of GF is usually as large as hundreds of micrometers, and the density is very low owing to the large pore size of the Ni foam catalyst skeletons, resulting in a large thermal resistance of the heat transfer from the PCM inside the large pore to the GF strut walls. Therefore, an approach to engineer the pore structure by growing a network of CNTs inside the pores, which further improves the thermal conductivity of the composite PCM compared with a composite PCM with only GF, was recently reported [1]. The pores of GF are large and open, which should also be optimized for the improvement of the shape stability of composite PCM.

Herein, we report another approach for further enhancing the conductive path of GF by filling the large pores of GF with a denser interconnected hollow graphene network (HGN). The obtained GF filled with the HGN, which is called hierarchical GF (HGF), was integrated with paraffin wax (PW) via vacuum impregnation to obtain a PW/HGF composite PCM. The HGN grown from the Ni powders acted as high-heat transfer fins between the GF skeletons and the inner spaces of pores to reduce the thermal resistance inside the GF pores. Hence, the HGF caused the PW/HGF composite PCM to have a higher thermal conductivity than the PW/GF composite PCM, with negligible impacts on other thermophysical properties. Compared with GF, HGF is more effective for overcoming the leakage problem of PW, which is a common problem for organic PCMs above the melting point, limiting their applications. This indicates that PW/HGF has a better shape-stabilization ability than organic PCMs because of the novel denser 3D network structure. Solar energy is a renewable and clean energy source of sufficient scale to replace fossil fuels, and various emerging carbon nanomaterials have been studied for the efficient energy conversion and storage of solar irradiation because of their unique structure and properties for sunlight absorption and conversion [11, 19–21]. We find that HGF also serves as a photon antenna that realizes photon capture and light-to-thermal energy conversion. Upon solar irradiation, the PW/HGF composite PCM can harvest sunlight and convert solar energy to thermal energy, which is then stored in the composite PCM with a high energy storage density.

2 Experimental

2.1 Fabrication of HGF, GF, and composite PCMs

The HGF was grown on a modified Ni foam template that was prepared by filling Ni powders (Sinopharm Chemical Reagent Co., Ltd., 200 mesh) into Ni foam

(Jilin Zhuoer Metal Materials Co., Ltd., 130 PPI, thickness of 5 mm) using a CVD method. The modified Ni foam template was prepared as follows. First, Ni powders were added to a poly(methyl methacrylate) (PMMA) solution (PMMA with molecular weight = 350,000, Aldrich, 4 wt.% in anisole), and the mixture was mechanically stirred to obtain a Ni powder/PMMA slurry. Second, Ni foam was immersed into the slurry to impregnate the Ni foam with the Ni powders. Finally, the as-prepared Ni foam filled with the Ni powder/PMMA slurry was baked at 180 ℃ for 3 h to obtain modified Ni foam templates.

The modified Ni foam templates were used as catalyst and 3D scaffold templates for the CVD growth of HGF. They were placed in a quartz tube with an outer diameter of 50 mm and inner diameter of 22 mm, which was pumped to a pressure of 4×10^{-3} Torr and then backfilled with a gas mixture of Ar (500 standard cubic centimeters per minute (sccm)) and H_2 (200 sccm) until atmospheric pressure was reached. The modified Ni foam templates were then heated to 1,000 ℃ under a flow of the mixed gas at atmospheric pressure in the furnace and annealed for 25 min to clean their surfaces and eliminate the surface oxide layer. CH_4 with a flow rate of 10 sccm was then introduced into the gas mixture. After the reaction-gas mixture flow, the samples were rapidly cooled to room temperature under a gas mixture of Ar (500 sccm) and H_2 (200 sccm) to obtain a modified Ni foam template covered with graphene (Ni-G). To prevent the structural collapse of HGF when nickel was etched away, the Ni-G was drop-coated with the PMMA solution (4 wt.% in anisole) and then baked at 180 ℃ for 3 h to form a coated PMMA layer acting as a support to reinforce the graphene structure. Then, the Ni foam templates were etched in a 3 M HCl solution at 80 ℃ overnight to obtain HGF-PMMA. Finally, freestanding HGF was obtained by dissolving the PMMA layer with acetone at 55 ℃. For comparison, the original Ni foam was also used as 3D scaffold templates for the CVD growth of GF.

The composite PCMs were prepared by a vacuum-impregnation method. PW was heated to 80 ℃ to melt, and the HGF and GF were immersed into the melted PW. The samples were then placed in a vacuum oven at 80 ℃ to remove air bubbles, followed by cooling to room temperature.

2.2 Characterization and measurements

The morphologies and surface elements of the samples were characterized using a field-emission scanning electron microscope (Zeiss Ultra 55, German, 10 kV) equipped with an X-ray detector for energy-dispersive X-ray spectroscopy (EDX) microanalysis. Raman spectra (excited at 638 nm) were obtained using a laser Raman spectrometer (XploRA, HORIBA Jobin Yvon, France). Transmission electron microscopy (TEM) was performed using a FEI Tecnai G2 F20 S-Twin microscope operated at an accelerating voltage of 200 kV. The samples were prepared by ultrasonication for ~30 min and then dropped onto a microgrid. Shape-stability measurements were performed using a thermomechanical analyzer (SDTS841e, Mettler Toledo, Switzerland). In addition, the shape stability was investigated by observing the samples at different temperatures. The samples were placed on a hot stage with increasing temperature, and corresponding digital photographs were taken. The thermal conductivity was measured using a Hot Disk Thermal Constant Analyzer (TPS 2500, Hot Disk AB Company, Sweden) by a transient plane heat source method. An infrared camera (Ti27, Fluke, USA) was used to record the heat transfer of the samples, which were placed on a hot stage with a constant temperature. The phase-change temperatures and phase-change enthalpies of the samples sealed in an aluminum pan were obtained by differential scanning calorimetry (DSC) using a TA Q20 instrument (USA) with a heating/cooling rate of 10 ℃/min in a highly purified nitrogen atmosphere. Fourier-transform infrared (FTIR) spectroscopy was performed using a Nicolet 6700 FTIR spectrometer (Nicolet Instrument Company, USA) with a resolution of 4 cm^{-1} in the transmission mode. A light-to-thermal energy conversion test was performed under simulated sunlight provided by a CEL-HXUV300 xenon lamp with an AM 1.5 filter, and the light irradiation power was verified using a CEL-NP2000 optical power meter (CEAULIGHT, China). The samples were placed in a foam box and irradiated under the simulated sunlight, and the temperature was recorded using a paperless

recorder with thermocouples (OMEGA). The optical properties of the samples were studied using an ultraviolet–visible–near-infrared (UV–vis–NIR) spectrophotometer (Lambda 750, Perkin-Elmer, USA) with an integrating sphere.

3 Results and discussion

3.1 Synthesis of HGF and composite PCMs

HGF was fabricated using a modified Ni foam template-assisted CVD method. As shown in Fig. 1, the synthesis strategy for HGF involves the preparation of a modified Ni foam template obtained by filling Ni powders into the Ni foam, followed by CVD growth and chemical etching of the modified Ni foam template. Then, the as-prepared HGF was immersed in melted PW in vacuum to obtain the composite PCM. Figure 2 shows the photographs of the samples obtained in each step.

As shown in the scanning electron microscopy (SEM) image of Fig. 3(a), the original Ni foam template exhibited a macro-porous structure with a pore size of several hundreds of micrometers. After CVD growth and etching, the obtained GF (Fig. 3(b)) copied and inherited the interconnected 3D macro-porous structure of Ni foam template. In contrast, the modified Ni foam template had a much denser porous structure (Fig. 3(d)), in which Ni powders were packed tightly within the pores fixed by PMMA (Figs. 2(b) and 3(g)). After the annealing and CVD growth, the original Ni powders merged together, forming high-density macro-porous Ni foams covered by a continuous layer of graphene (Figs. 2(c) and 3(e)). After the etching of the Ni template, freestanding HGF—a monolith of

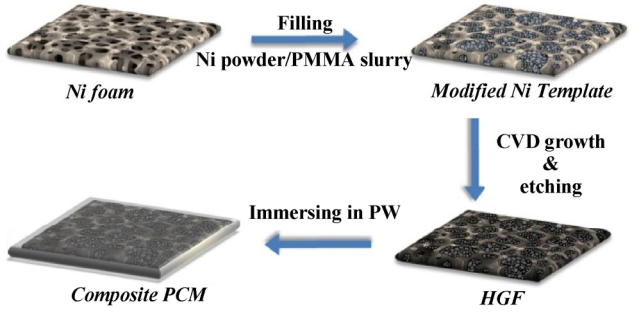

Figure 1 Schematic illustration of synthesis of HGF and PCM.

an interconnected graphene 3D network—was obtained (Figs. 2(f) and 3(f)). Compared with GF (Fig. 3(b)), the pores of the HGF were filled with a denser graphene network (Fig. 3(c)). The interconnected graphene network was composed of hollow spherical graphene (Fig. 3(i)), which was copied from the shape of the Ni powers after annealing and benefited the encapsulation of the PW to form the core–shell structure. The HGN inside GF caused a denser network and an improved thermal conductive path and shape stability of HGF.

The HGF was characterized by Raman spectroscopy to evaluate the quality and film thickness of graphene (Fig. 4(a)). The defect-related D band was strongly suppressed in both the GF area growing from Ni foam and the HGN area growing from Ni powders, indicating the overall high quality of the HGF samples [21]. The number of graphene layers in different areas of the HGF was estimated according to the 2D band full width at half maximum and the intensity ratio of the 2D band to the G band [22], which shows that monolayer and multilayer graphene coexisted in the HGN area and that multilayer graphene existed in the GF area.

TEM measurements (Figs. 4(b) and 4(c)) reveal a curved sheet-like morphology of building blocks in the freestanding HGF (Fig. 4(d)). All of the Ni template was removed, which was confirmed by EDX (Fig. 4(b)). High-resolution TEM images indicate that the HGF had a high-quality graphitic layer structure with 1 to 13 layers, which accords with the Raman results. The non-uniformity of the layer numbers is attributed to the polycrystalline nature of Ni, whereby individual Ni grains may have independently affected the thickness of the graphene film during CVD [23].

To examine the performance of its application in composite PCMs, we prepared a PW/HGF composite PCM (Fig. 4(g)) using a vacuum-impregnation method. For comparison, a PW/GF composite PCM was also prepared by the same process. SEM images of the PW/GF (Fig. 4(e)) and PW/HGF (Fig. 4(f)) composite PCMs show that the pores of the GF and HGF were fully filled with PW and that the PW combined compactly with the GF and HGF. The foam-like networks of the GF and HGF remained in the composite PCMs. Compared with the PW/GF composite PCM (Fig. 4(e)),

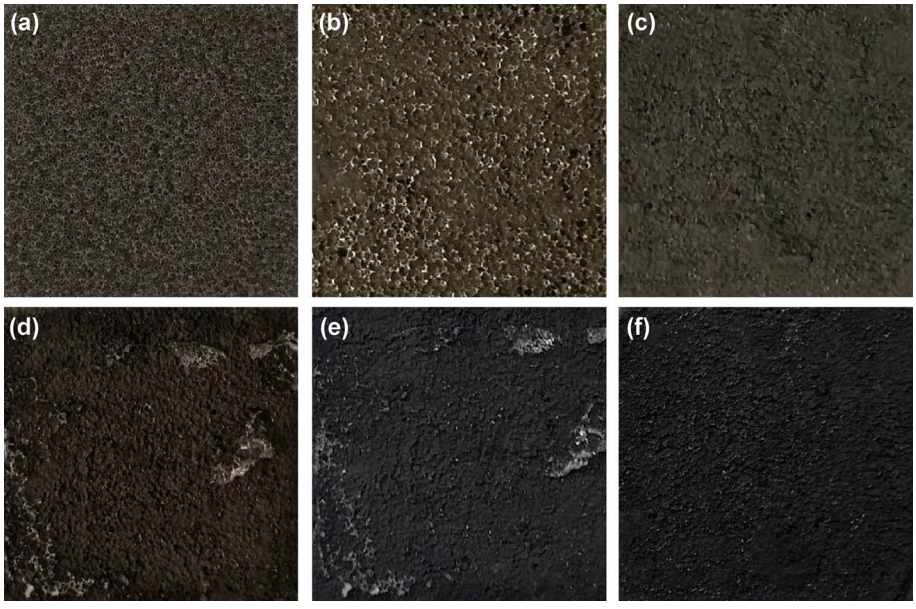

Figure 2 Photographs of the samples obtained in each step. (a) Ni foam, (b) modified Ni template, (c) Ni-G, (d) Ni-G-PMMA, (e) HGF-PMMA, and (f) HGF.

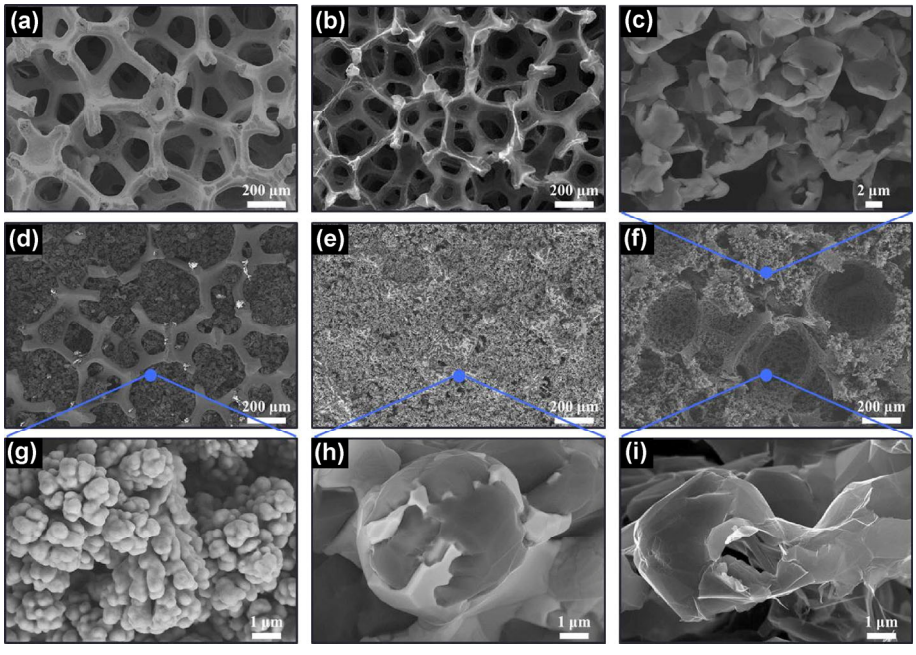

Figure 3 SEM images of (a) Ni foam, (b) GF, (c) HGN, (d) modified Ni template, (e) CVD growth of graphene film on modified Ni template (Ni-G), (f) HGF, (g) Ni powders filling in the Ni foam, (h) graphene growing on the Ni powder, and (i) enlarged hollow graphene of HGN.

a substantially denser network is observed in the PW/HGF composite PCM (Fig. 4(f)).

3.2 Shape-stabilization of PW and composite PCMs

The shape stability of PCMs is of great importance for preventing leakage at temperatures above the melting point of the working substance. The shape stabilities of the PCMs were characterized by thermomechanical analysis (TMA) and digital-camera observation. As shown in Fig. 5(a), pure PW could

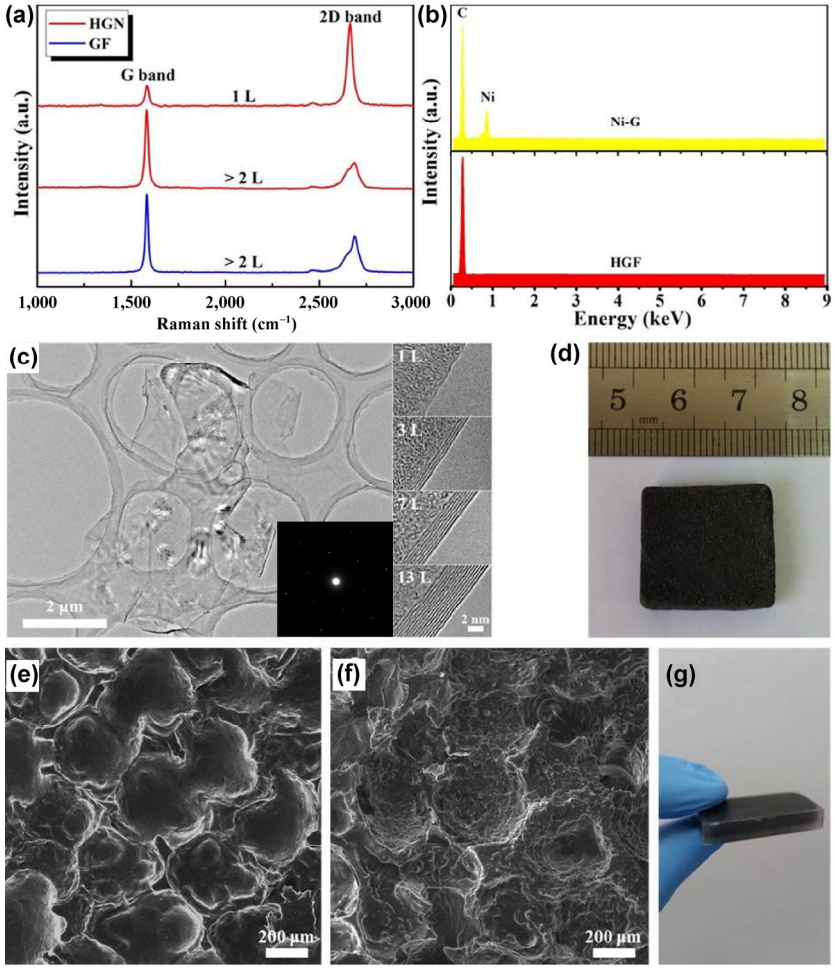

Figure 4 (a) Raman spectra of HGF obtained for different areas. Red and blue spectra correspond to HGN growing on Ni powders and GF growing on Ni foam, respectively. (b) EDX spectra of Ni-G and HGF. (c) TEM image of graphene layers in HGF. The insets show the electron-diffraction patterns and high-resolution TEM images of graphene layers with a single layer (1 L), three layers (3 L), seven layers (7 L), and thirteen layers (13 L), from top to bottom. (d) Photograph of freestanding HGF. SEM images of (e) the PW/GF composite PCM and (f) the PW/HGF composite PCM. (g) Photograph of a PW/HGF composite PCM.

not retain its original shape, and its dimensions started to decrease at ~40 ℃. The dimensions decreased remarkably as the temperature increased. At a temperature higher than 65 ℃, a solid–liquid phase change occurred, causing the pure PW sample to leak completely. In contrast, the dimensions of the PW/GF and PW/HGF composite PCMs were maintained at a temperature above 90 ℃, which is far higher than the melting point of pure PW. Therefore, the composite PCMs remained in the solid state during the phase change, owing to the supporting effect of the 3D foam-like structure and the good wettability of PW in graphene networks.

The PW/HGF composite PCM with a double network structure had better shape stability than the PW/GF composite PCM (inset of Fig. 5(a)). The HGF had a substantially denser network structure than the GF. In addition to the supporting effect of the GF framework, the HGN inside the GF framework (Fig. 2(i)), which had hollow shell structures and played the role of packaging PW in these shells to form the core–shell structure, contributed to the shape stability of the PW/HGF composite PCM. To examine the shape stability of each sample, the samples were heated to different temperatures and recorded by a digital camera. Figure 5(b) shows that all the samples were in a solid state and had a square shape at 30 ℃. At 65 ℃, which is ~15 ℃ higher than the melting

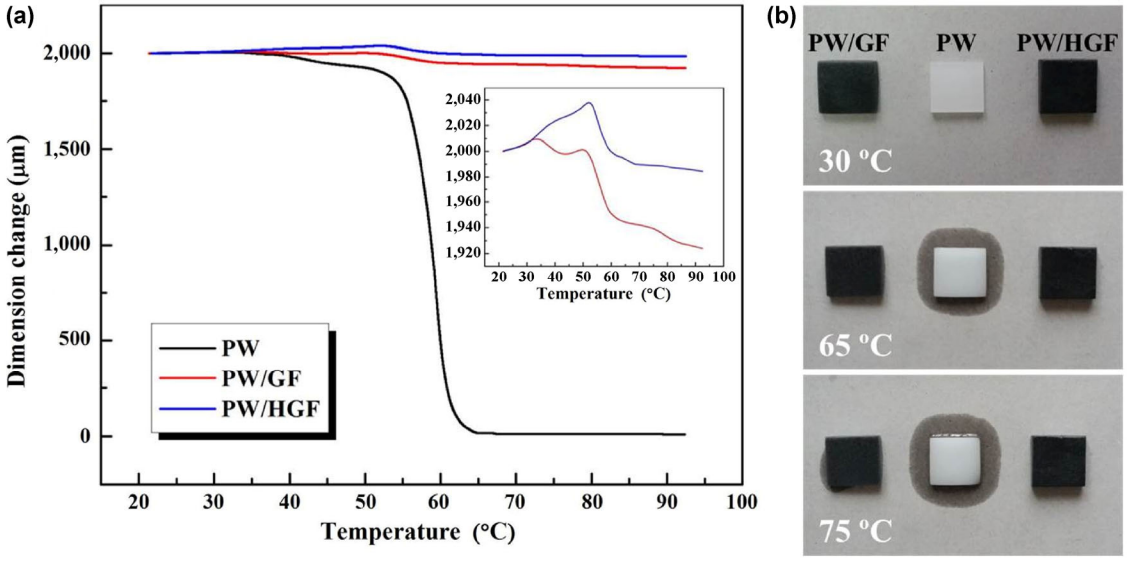

Figure 5 (a) TMA curves of pure PW, PW/GF composite, and PW/HGF composite PCMs. (b) Photographs of the pure PW, PW/GF composite, and PW/HGF composite PCMs at different temperatures.

point of PW, the pure PW sample started to melt, with obvious leakage, while both the PW/GF and PW/HGF composite PCMs remained stable, without any trace of liquid leakage. When the temperature increased to 75 °C, the pure PW sample had more leakage, and the PW/GF composite PCM started to undergo slight leakage. However, the PW/HGF composite PCM maintained its original shape without any leakage, which is consistent with the TMA results.

3.3 Heat-transfer properties of PW and composite PCMs

Figure 6(a) shows the thermal conductivity of pure PW, and the PW/GF and PW/HGF composite PCMs, which are 0.27, 1.22, and 2.28 W/mK, respectively. The thermal conductivity of the PW/HGF composite PCM was 87% higher than that of the PW/GF composite PCM and 744% that of pure PW. Thus, the foam-like 3D graphene macrostructures provided a highly efficient thermal transport pathway, causing a dramatic increase in the thermal conductivity of the PCMs. The HGN inside the GF framework of the HGF provided a substantially denser thermal conductive pathway, which contributed to a great enhancement in the thermal transport and an obvious reduction in the thermal resistance compared with PW and graphene networks. Therefore, the PW/HGF composite

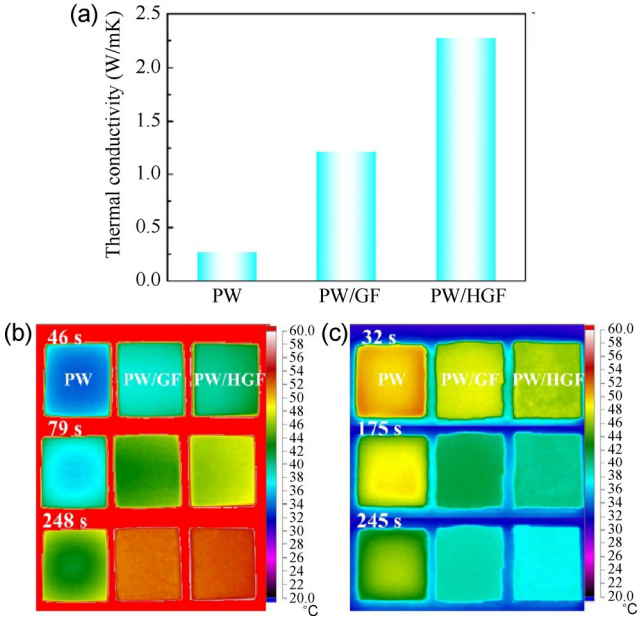

Figure 6 (a) Thermal conductivities of pure PW, PW/GF, and PW/HGF composite PCMs. Thermal transport evolution of pure PW, PW/GF, and PW/HGF composite PCMs during (b) heating and (c) cooling.

PCM had a greatly improved thermal conductivity, which further shortened the time needed for heat storage and release.

To reveal the heat-transfer rate during thermal energy storage and release, an infrared camera was used to record the transient temperature response

during heating and cooling. During heating, samples were put on an isothermal hot plate with a constant temperature of 70 ℃, and temperature-distribution images taken at different time are shown in Fig. 6(b). The color of the PW/GF and PW/HGF composite PCMs changed far faster than that of pure PW, which indicates that 3D interconnected graphene materials improve the thermal transport of PW based PCMs remarkably. Furthermore, the temperature increase was even faster in the PW/HGF composite PCM, indicating a higher rate of thermal response than the PW/GF composite PCM. The same phenomenon has also been observed in the cooling process (Fig. 6(c)). The high thermal conductivity of PW/HGF provides a fast heat-transfer rate, enabling PW/HGF to absorb thermal energy rapidly during phase change. The aforementioned results provide strong evidence that the HGF with a novel hierarchical structure led to a remarkable enhancement of the thermal transport properties of the PW based PCM, highlighting its potential to improve the working efficiency of PCMs.

3.4 Thermophysical properties of PW and composite PCMs

The phase-change enthalpy, which reflects the thermal energy storage capacity, is another critical parameter for evaluating the performance of PCMs. In the DSC heating and cooling curves of pure PW, PW/GF, and PW/HGF composite PCMs in Fig. 7(a), two main transition peaks are clearly observed. The sharp or main peak is attributed to the heterogeneously nucleated rotator-liquid phase transition, which represents the solid–liquid phase change of paraffin, and the minor peak at the left side of the sharp peak corresponds to the homogeneously nucleated crystal-rotator phase transition, which represents the solid–solid phase transition of paraffin [24]. The thermal energy storage data obtained from the DSC curves, such as onset melting/crystallization temperature (T_{mo}/T_{co}), end melting/crystallization temperature (T_{me}/T_{ce}), peak melting/crystallization temperature (T_{mp}/T_{cp}), and melting/ crystallization enthalpy of composite PCMs (ΔH_{mc}/ΔH_{cc}), are listed in Table 1. A negligible change in the phase-change temperatures was observed for a PW/GF composite PCM with T_{mp} of 56.8 ℃ and a PW/HGF composite PCM with T_{mp} of 56.8 ℃ compared with a pure PW PCM with T_{mp} of 56.5 ℃. Moreover, the PW/GF and PW/HGF composite PCMs exhibited high thermal energy storage densities. Generally, the thermal energy storage density of composite PCMs is degraded with the incorporation of fillers because of the increased replacement of the working substance with fillers [25]. Nevertheless, the thermal energy storage densities of PW/GF and PW/HGF composite PCMs reached as high as 99.6% and 95.2% of pure PW, respectively. The phase-change enthalpy of the PW/HGF composite PCM was slightly lower than that of the PW/GF composite PCM. Compared with GF, which has a macro-porous network structure, HGF has a double-network structure comprising the GF framework and a denser HGN, and the HGN inside the GF framework not only further improves the thermal conductivity but also replaces a fraction of PW—the working substance—in the PW/HGF composite PCM, resulting in a lower phase-change enthalpy than the PW/GF composite PCM. The properties shown are superior enough for PW/HGF composite PCMs to be used as efficient PCMs for thermal-energy storage.

3.5 Thermal reliability of PW/HGF composite PCMs

Reliability and stability are main issues for PCMs after long-term usage, and they must be stable in terms of the thermal properties and chemical structures. The stability of the thermal performances of the PW/HGF composite PCM was determined by performing DSC

Table 1 Phase-change behavior of the pure PW, PW/GF, and PW/HGF composite PCMs

Samples	T_{co} (℃)	T_{ce} (℃)	T_{cp} (℃)	ΔH_{cc} (J/g)	T_{mo} (℃)	T_{me} (℃)	T_{mp} (℃)	ΔH_{mc} (J/g)
PW	53.3	36.7	48.0	157.0	47.2	61.2	56.5	160.9
PW/GF	53.3	39.3	47.8	156.5	47.4	61.2	56.8	160.2
PW/HGF	53.2	39.5	47.7	151.1	47.2	60.8	56.8	153.1

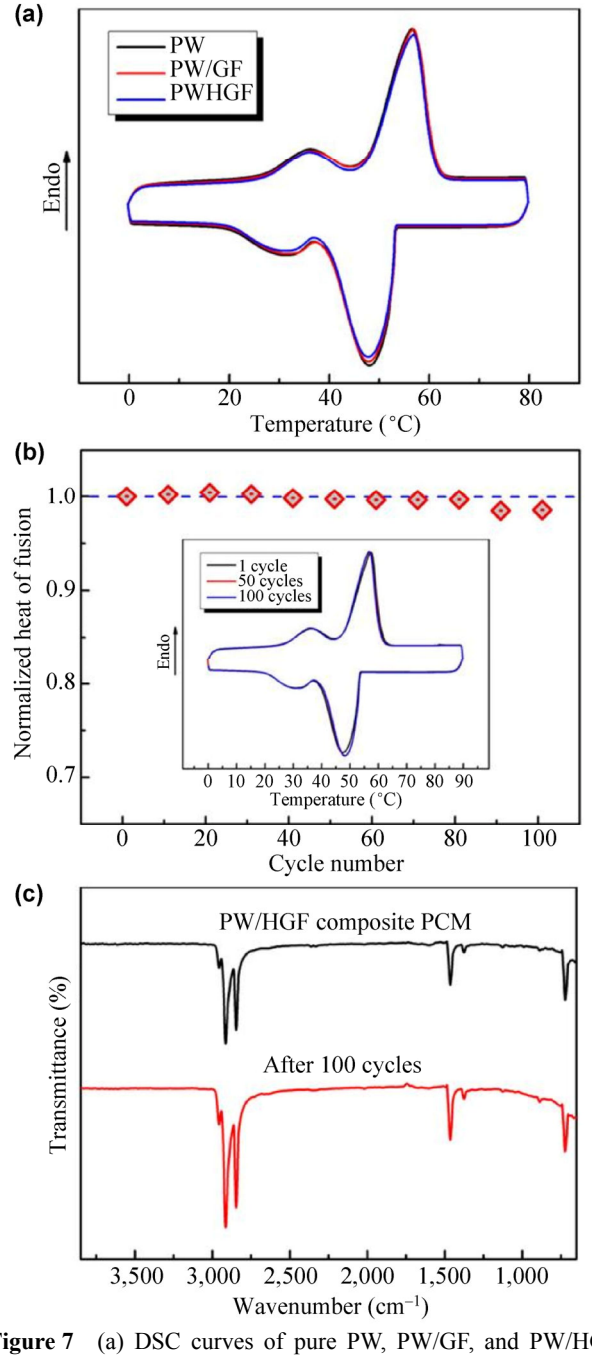

Figure 7 (a) DSC curves of pure PW, PW/GF, and PW/HGF composite PCMs. (b) The obtained mass specific heat of fusion normalized by the first heating cycle of the PW/HGF composite PCM. The inset shows the DSC curves of the PW/HGF composite PCM cycled 100 times. (c) FTIR spectra of the PW/HGF composite PCM before and after 100 thermal cycles.

thermal cycling tests. Figure 7(b) shows the DSC curves of the PW/HGF composite PCM after 1, 50, and 100 thermal cycles, and the phase-change temperatures changed negligibly. Only a slight reduction in the heat of fusion was observed over 100 solid–liquid phase transition cycles for the PW/HGF composite PCM, as shown in the heat of fusion normalized by the first heating cycle of the PW/HGF composite PCM. The small reduction in the heat of fusion for the sample is attributed to PCM evaporation and mass loss during the DSC cycling measurement, which was performed under a constant flow of dry nitrogen gas. Such losses are not present in a practical thermal storage device where the PCM is enclosed inside a container [5].

Figure 7(c) shows the FTIR spectra of the PW/HGF composite PCM before and after 100 thermal cycles. No changes in the shape or position of the characteristic peaks were observed after thermal cycling, which indicates that the chemical structure of the PW/HGF composite PCM was stable after 100 melting and cooling cycles. According to the aforementioned results, the PW/HGF composite PCM had a superior comprehensive performance, as well as good thermal reliability and chemical stability.

3.6 Solar-to-thermal energy conversion

The energy storage of PCMs has been realized by electro-heat or photo-thermal routes in recent studies [3, 10, 20, 26–28]. In our work, solar radiation was utilized to drive the energy conversion and storage in composite PCMs. The incident light-to-thermal energy conversion behavior of PW, PW/GF, and PW/HGF composite PCMs were investigated by simulated solar illumination (AM 1.5) at a constant intensity of 100 mW/cm^2, and the temperature evolution of the samples was recorded by a paperless recorder with thermocouples, as illustrated in Fig. 8(a). The light-to-thermal energy conversion spectra of the samples are shown in Fig. 8(b). Compared with pure PW, the temperature of the PW/GF and PW/HGF composite PCMs increased more rapidly upon solar irradiation. As irradiation time increased, the temperature growth plateau of the composite PCMs appeared between approximately 48 and 56 °C, which indicates the solid–liquid phage change of composite PCMs upon light irradiation. When the PW/GF and PW/HGF composite PCMs were exposed to the light radiation, they absorbed the radiation and converted it to thermal energy, followed by storing the thermal energy in composite PCMs. After the light irradiation was removed, the temperatures of the PW/GF and PW/HGF

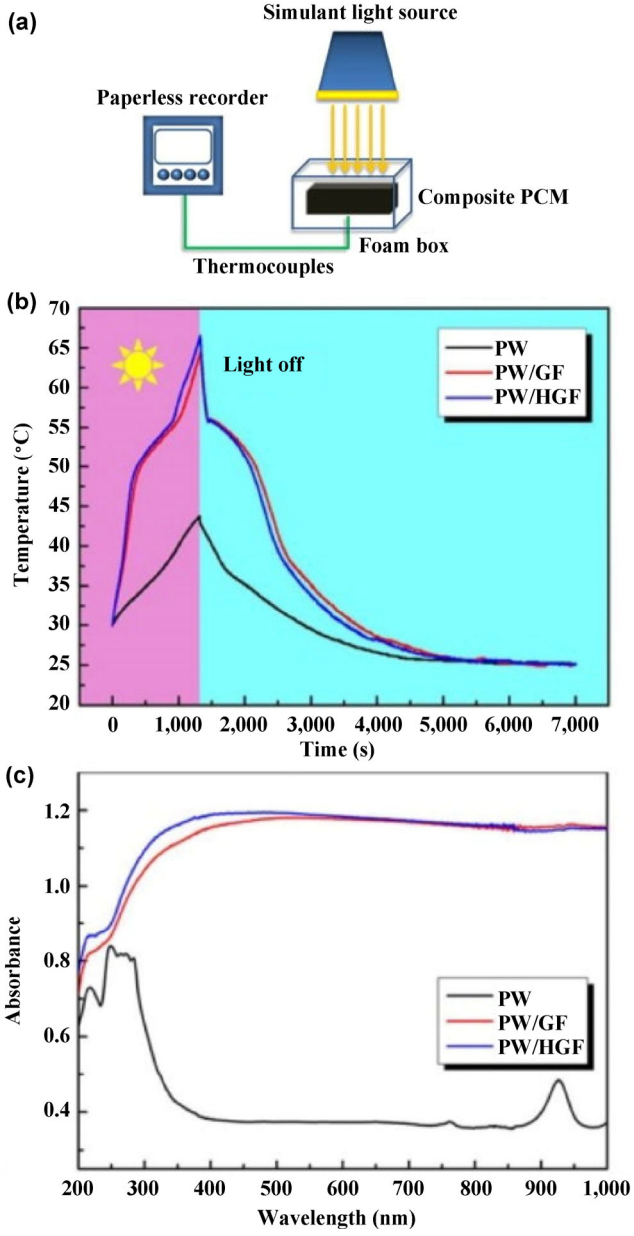

Figure 8 (a) Schematic of the light-to-thermal energy conversion and storage measuring system. (b) Light-to-thermal energy conversion curves for pure PW, PW/GF, and PW/HGF composite PCMs. (c) UV–vis–NIR absorption spectrum for pure PW, PW/GF, and PW/HGF composite PCMs.

composite PCMs decreased rapidly and then exhibited a freezing plateau between approximately 55 and 50 ℃, indicating that a large amount of thermal energy is released by the composite PCMs in the cooling phase-change process. In contrast, no visible melting or cooling plateaus were observed for the pure PW, which means that the phase change did not occur upon light irradiation.

The light-to-thermal energy conversion phenomenon of composite PCMs should be related to their effective absorption of light. Thus, the UV–vis–NIR absorption spectra of samples were obtained, as shown in Fig. 8(c). The PW/GF and PW/HGF composite PCMs exhibit total absorbance over the whole UV–vis–NIR range, while the pure PW shows no absorption peak in the visible-light range. The black color of the HGF gave it ideal light absorbance, which enhanced the photoabsorption of the composite PCMs. The light-to-thermal energy conversion and thermal energy storage efficiency (η) of the composite PCMs can be estimated according to the ratio of heat stored in the composite PCMs, with respect to the light radiation energy received during the phase-change period [3, 10]. The calculation can be performed using the following equation

$$\eta = m \cdot \Delta H / (P \cdot S \cdot (t_0 - t_e)) \quad (1)$$

where m is the total mass of the sample, ΔH is the phase-change enthalpy obtained by DSC, P is the light irradiation intensity of simulated light source (100 mW/cm^2 @ AM1.5), S is the surface area of the sample, and t_0 and t_e are the light-driven phase-change time of the sample before and after the phase change.

According to Eq. (1), the η of the PW/GF and PW/HGF composite PCMs were calculated to be approximately 88% and 89%, respectively, showing that HGF is an effective photon captor and molecular heater and enabled the PW/HGF composite PCM to absorb light radiation and convert it to thermal energy, followed by storing the thermal energy.

4 Conclusions

A versatile modified template-directed CVD method is proposed to prepare a kind of novel 3D graphene hierarchical macrostructure with a double-network structure, the GF framework, and a denser HGN, by filling the large pores of GF with interconnected HGN. When integrated with PW, the PW/HGF composite PCM exhibited a substantially higher thermal conductivity and better shape stability than the PW/GF composite PCM. The improved thermal transport property of the PW/HGF composite PCM is attributed

to the HGN, the enhanced conductive pathway inside the GF, which also led to better shape stability due to the package effect of hollow graphene on PW. Furthermore, PW/HGF composite PCM showed a high thermal energy storage density and good thermal reliability and chemical stability. The thermal-energy storage of the PW/HGF composite PCM was driven by light irradiation, and the PW/HGF composite PCM demonstrated a total absorbance over the whole UV–vis–NIR range, along with high light-to-thermal energy conversion and storage efficiencies. The present study represents an important step toward the development of high-performance composite PCMs with a novel hierarchical structure for thermal management and thermal-energy conversion and storage applications.

Acknowledgements

This work was funded by the National Thousand Young Talents of China, the National Natural Science Foundation of China (Nos. 21544001, 21603038, 51422305, and 51421061), the Innovation Team Program of Science & Technology Department of Sichuan Province (No. 2014TD0002) and State Key Laboratory of Polymer Materials Engineering (No. sklpme2014-2-02).

References

[1] Kholmanov, I.; Kim, J.; Ou, E.; Ruoff, R. S.; Shi, L. Continuous carbon nanotube–ultrathin graphite hybrid foams for increased thermal conductivity and suppressed subcooling in composite phase change materials. *ACS Nano* **2015**, *9*, 11699–11707.

[2] Zhang, Z. Y.; Dong, Y.; Wang, L.; Wang, S. Scalable synthesis of a Pd nanoparticle loaded hierarchically porous graphene network through multiple synergistic interactions. *Chem. Commun.* **2015**, *51*, 8357–8360.

[3] Chen, L.; Zou, R.; Xia, W.; Liu, Z.; Shang, Y.; Zhu, J.; Wang, Y.; Lin, J.; Xia, D.; Cao, A. Electro- and photodriven phase change composites based on wax-infiltrated carbon nanotube sponges. *ACS Nano* **2012**, *6*, 10884–10892.

[4] Liu, Z. P.; Zou, R. Q.; Lin, Z. Q.; Gui, X. C.; Chen, R. J.; Lin, J. H.; Shang, Y. Y.; Cao, A. Y. Tailoring carbon nanotube density for modulating electro-to-heat conversion in phase change composites. *Nano Lett.* **2013**, *13*, 4028–4035.

[5] Ji, H. X.; Sellan, D. P.; Pettes, M. T.; Kong, X. H.; Ji, J. Y.; Shi, L.; Ruoff, R. S. Enhanced thermal conductivity of phase change materials with ultrathin-graphite foams for thermal energy storage. *Energy Environ. Sci.* **2014**, *7*, 1185–1192.

[6] Ye, S. B.; Zhang, Q. L.; Hu, D. D.; Feng, J. C. Core-shell-like structured graphene aerogel encapsulating paraffin: Shape-stable phase change material for thermal energy storage. *J. Mater. Chem. A* **2015**, *3*, 4018–4025.

[7] Zhang, Q. L.; Cui, K. P.; Feng, J. C.; Fan, J. S.; Li, L. B.; Wu, L. M.; Huang, Q. Investigation on the recovery performance of olefin block copolymer/hexadecane form stable phase change materials with shape memory properties. *Sol. Energy Mater. Sol. Cells* **2015**, *132*, 632–639.

[8] Xin, G.; Sun, H.; Scott, S. M.; Yao, T.; Lu, F.; Shao, D.; Hu, T.; Wang, G.; Ran, G.; Lian, J. Advanced phase change composite by thermally annealed defect-free graphene for thermal energy storage. *ACS Appl. Mater. Interfaces* **2014**, *6*, 15262–15271.

[9] Goli, P.; Legedza, S.; Dhar, A.; Salgado, R.; Renteria, J.; Balandin, A. A. Graphene-enhanced hybrid phase change materials for thermal management of Li-ion batteries. *J. Power Sources* **2014**, *248*, 37–43.

[10] Wang, Y. M.; Tang, B. T.; Zhang, S. F. Single-walled carbon nanotube/phase change material composites: Sunlight-driven, reversible, form-stable phase transitions for solar thermal energy storage. *Adv. Funct. Mater.* **2013**, *23*, 4354–4360.

[11] Yu, Z.-T.; Fang, X.; Fan, L.-W.; Wang, X.; Xiao, Y.-Q.; Zeng, Y.; Xu, X.; Hu, Y.-C.; Cen, K.-F. Increased thermal conductivity of liquid paraffin-based suspensions in the presence of carbon nano-additives of various sizes and shapes. *Carbon* **2013**, *53*, 277–285.

[12] Qi, G.-Q.; Yang, J.; Bao, R.-Y.; Liu, Z.-Y.; Yang, W.; Xie, B.-H.; Yang, M.-B. Enhanced comprehensive performance of polyethylene glycol based phase change material with hybrid graphene nanomaterials for thermal energy storage. *Carbon* **2015**, *88*, 196–205.

[13] Zhou, M.; Lin, T. Q.; Huang, F. Q.; Zhong, Y. J.; Wang, Z.; Tang, Y. F.; Bi, H.; Wan, D. Y.; Lin, J. H. Highly conductive porous graphene/ceramic composites for heat transfer and thermal energy storage. *Adv. Funct. Mater.* **2013**, *23*, 2263–2269.

[14] Chen, Z. P.; Ren, W. C.; Gao, L. B.; Liu, B. L.; Pei, S. F.; Cheng, H. M. Three-dimensional flexible and conductive interconnected graphene networks grown by chemical vapour deposition. *Nat. Mater.* **2011**, *10*, 424–428.

[15] Worsley, M. A.; Pauzauskie, P. J.; Olson, T. Y.; Biener, J.; Satcher, J. H., Jr.; Baumann, T. F. Synthesis of graphene aerogel with high electrical conductivity. *J. Am. Chem. Soc.* **2010**, *132*, 14067–14069.

[16] Li, Y. R.; Chen, J.; Huang, L.; Li, C.; Hong, J.-D.; Shi, G. Q. Highly compressible macroporous graphene monoliths via an improved hydrothermal process. *Adv. Mater.* **2014**, *26*, 4789–4793.

[17] Pettes, M. T.; Ji, H. X.; Ruoff, R. S.; Shi, L. Thermal transport in three-dimensional foam architectures of few-layer graphene and ultrathin graphite. *Nano Lett.* **2012**, *12*, 2959–2964.

[18] Sun, H.; Deng, J.; Qiu, L. B.; Fang, X.; Peng, H. S. Recent progress in solar cells based on one-dimensional nanomaterials. *Energy Environ. Sci.* **2015**, *8*, 1139–1159.

[19] Bonaccorso, F.; Balis, N.; Stylianakis, M. M.; Savarese, M.; Adamo, C.; Gemmi, M.; Pellegrini, V.; Stratakis, E.; Kymakis, E. Functionalized graphene as an electron-cascade acceptor for air-processed organic ternary solar cells. *Adv. Funct. Mater.* **2015**, *25*, 3870–3880.

[20] Li, Y. Q.; Samad, Y. A.; Polychronopoulou, K.; Alhassan, S. M.; Liao, K. From biomass to high performance solar-thermal and electric-thermal energy conversion and storage materials. *J. Mater. Chem. A* **2014**, *2*, 7759–7765.

[21] Kim, K. S.; Zhao, Y.; Jang, H.; Lee, S. Y.; Kim, J. M.; Kim, K. S.; Ahn, J. H.; Kim, P.; Choi, J. Y.; Hong, B. H. Large-scale pattern growth of graphene films for stretchable transparent electrodes. *Nature* **2009**, *457*, 706–710.

[22] Li, X. S.; Cai, W. W.; An, J.; Kim, S.; Nah, J.; Yang, D. X.; Piner, R.; Velamakanni, A.; Jung, I.; Tutuc, E. et al. Large-area synthesis of high-quality and uniform graphene films on copper foils. *Science* **2009**, *324*, 1312–1314.

[23] Reina, A.; Jia, X. T.; Ho, J.; Nezich, D.; Son, H. B.; Bulovic, V.; Dresselhaus, M. S.; Kong, J. Large area, few-layer graphene films on arbitrary substrates by chemical vapor deposition. *Nano Lett.* **2009**, *9*, 30–35.

[24] Mehrali, M.; Latibari, S. T.; Mehrali, M.; Metselaar, H. S. C.; Silakhori, M. Shape-stabilized phase change materials with high thermal conductivity based on paraffin/graphene oxide composite. *Energy Convers. Manag.* **2013**, *67*, 275–282.

[25] Yavari, F.; Fard, H. R.; Pashayi, K.; Rafiee, M. A.; Zamiri, A.; Yu, Z. Z.; Ozisik, R.; Borca-Tasciuc, T.; Koratkar, N. Enhanced thermal conductivity in a nanostructured phase change composite due to low concentration graphene additives. *J. Phys. Chem. C* **2011**, *115*, 8753–8758.

[26] Huang, X. Y.; Liu, Z. P.; Xia, W.; Zou, R. Q.; Han, R. P. S. Alkylated phase change composites for thermal energy storage based on surface-modified silica aerogels. *J. Mater. Chem. A* **2015**, *3*, 1935–1940.

[27] Chen, R. J.; Yao, R. M.; Xia, W.; Zou, R. Q. Electro/photo to heat conversion system based on polyurethane embedded graphite foam. *Appl. Energ.* **2015**, *152*, 183–188.

[28] Huang, X. Y.; Xia, W.; Zou, R. Q. Nanoconfinement of phase change materials within carbon aerogels: Phase transition behaviours and photo-to-thermal energy storage. *J. Mater. Chem. A* **2014**, *2*, 19963–19968.